



Title	Heterogeneous distribution of doublecortin-expressing cells surrounding the rostral migratory stream in the juvenile mouse
Author(s)	Aoyagi, Yuka; Hibi, Terumasa; Kimori, Yoshitaka; Sawada, Masato; Kawakami, Ryosuke; Sawamoto, Kazunobu; Nemoto, Tomomi
Citation	The journal of comparative neurology, 526(16), 2631-2646 https://doi.org/10.1002/cne.24521
Issue Date	2018-11-01
Doc URL	http://hdl.handle.net/2115/75999
Rights	This is the peer reviewed version of the following article: Yuka Aoyagi, Terumasa Hibi, Yoshitaka Kimori, Masato Sawada, Ryosuke Kawakami, Kazunobu Sawamoto and Tomomi Nemoto. Heterogeneous distribution of doublecortin expressing cells surrounding the rostral migratory stream in the juvenile mouse. The Journal of Comparative Neurology. Volume526, Issue16 (November 1, 2018). Pages 2631-2646, which has been published in final form at https://doi.org/10.1002/cne.24521 . This article may be used for non-commercial purposes in accordance with Wiley Terms and Conditions for Use of Self-Archived Versions.
Type	article (author version)
File Information	manuscript.pdf



[Instructions for use](#)

Heterogeneous distribution of doublecortin-expressing cells surrounding the rostral migratory stream in the juvenile mouse

Short running title: 3D distribution of Dcx-expressing cells

Yuka Aoyagi^{1,2}, Terumasa Hibi^{1,2}, Yoshitaka Kimori^{3†}, Masato Sawada⁴, Ryosuke Kawakami^{1,2,‡}, Kazunobu Sawamoto^{4,5}, Tomomi Nemoto^{1,2,*}

¹Graduate School of Information Science and Technology, Hokkaido University, Sapporo, Hokkaido 060-0814, Japan

²Research Institute for Electronic Science, Hokkaido University, Sapporo, Hokkaido 001-0020, Japan

³Imaging Science Division, Center for Novel Science Initiatives, National Institutes of Natural Sciences, Okazaki, Aichi 444-8787, Japan

⁴Department of Developmental and Regenerative Biology, Nagoya City University Graduate School of Medical Sciences, Nagoya, Aichi 467-8601, Japan

⁵Division of Neural Development and Regeneration, National Institute for Physiological Sciences, Okazaki, Aichi 444-8585, Japan

† Present affiliation: Department of Management and Information Sciences, Faculty of Environmental and Information Sciences, Fukui University of Technology, Fukui, Fukui 910-8505, Japan

‡ Present affiliation: Department of Molecular Medicine for Pathogenesis, Ehime University Graduate School of Medicine, Toon, Ehime 791-0295, Japan

*** Corresponding author:**

Tomomi Nemoto

Laboratory of Molecular and Cellular Biophysics,
Research Institute for Electronic Science, Hokkaido University
Kita 21 Nishi 10, Kita-ku, Sapporo 001-0021, Japan

Phone: +81 11 706 9362,

Fax: +81 11 706 9363

Email: tn@es.hokudai.ac.jp

Acknowledgments

We are grateful to Dr. K. Iijima and Dr. K. Otomo, Research Institute for Electronic Science, Hokkaido University, for their helpful advice. We are also grateful to H. Osanai, Graduate School of Information Science and Technology, Hokkaido University, for his technical support and helpful advice. This work was supported by Grant-in-Aid for JSPS Research Fellows (26-1533), NIBB Collaborative Research Program (15-406, 16-530, 17-517), the Research Program of “Five-star Alliance” in “NJRC Mater. & Dev.”, MEXT KAKENHI Grant Number JP 15H05953 “Resonance Bio,” and Brain/MINDS, AMED, Japan.

Abstract

In the postnatal mammalian brain, neural stem cells of the ventricular–subventricular zone continue to generate doublecortin (Dcx)-expressing immature neurons.

Throughout life, these immature neurons migrate to the olfactory bulb through the rostral migratory stream (RMS). In this study, we investigated the distribution of these putative immature neurons using enhanced green fluorescent protein (EGFP) expression in the area surrounding the RMS of the juvenile *Dcx-EGFP* mice. Through the combined use of an optical clearing reagent (a 2,2'-thiodiethanol solution) and two-photon microscopy, we visualized three-dimensionally the EGFP-positive cells in the entire RMS and its surroundings. The resulting wide-field and high-definition images along with computational image processing methods developed in this study were used to comprehensively determine the position of the EGFP-positive cells. Our findings revealed that the EGFP-positive cells were heterogeneously distributed in the area surrounding the RMS. In addition, the orientation patterns of the leading process of these cells, which displayed the morphology of migrating immature neurons, differed depending on their location. These novel results provide highly precise morphological information for immature neurons and suggest that a portion of immature neurons may be detached from the RMS and migrate in various directions.

Keywords: neurogenesis, neural stem cells, multiphoton fluorescence microscopy, three-dimensional imaging, computer-assisted image processing, RRID: AB_561007, RRID: AB_477010, RRID: AB_2298772, RRID: AB_591819, RRID: AB_664697, RRID: AB_141708, RRID: AB_141637, RRID: AB_141607, RRID: AB_141633

1. Introduction

In the postnatal mammalian brain, neurogenesis continuously occurs throughout life in two restricted regions, namely, the ventricular–subventricular zone (V-SVZ) of the lateral ventricle and the subgranular zone of the hippocampal dentate gyrus (Fuentelba, Obernier, & Alvarez-Buylla, 2012). In the V-SVZ, neural stem cells generate immature neurons, which later migrate via the rostral migratory stream (RMS), which represents a pathway to the olfactory bulb (OB) (Anton et al., 2004; García-González et al., 2017; Kaneko et al., 2010; Ota et al., 2014; Snayyan et al., 2009). These migrating immature neurons form elongated cell aggregates, termed chains, within the RMS (Lois, García-Verdugo, & Alvarez-Buylla, 1996). In addition, they display a long leading process, which forms a transient cytoplasmic dilation (referred to as a swelling) (Bellion, Baudoin, Alvarez, Bornens, & Métin, 2005; Schaar & McConnell, 2005). After reaching the OB, the immature neurons differentiate into mature neurons and subsequently integrate into olfactory circuits (García-González et al., 2017; Lois & Alvarez-Buylla, 1994; Luskin, 1993; Sawada et al., 2018). The V-SVZ-derived immature neurons can also migrate toward damaged regions, where they can contribute to neuronal regeneration (Arvidsson, Collin, Kirik, Kokaia, & Lindvall, 2002; Jinnou et al., 2018; Parent, Vexler, Gong, Derugin, & Ferriero, 2002; Yamashita et al., 2006; Yang et al.,

2007). Therefore, investigating migratory immature neurons in the postnatal brain is important for better understanding mechanisms underlying the maintenance of homeostasis and neuronal regeneration following injury.

Within the RMS and its surroundings, the V-SVZ-derived immature neurons, astrocytes, and blood vessels undergo postnatal structural reorganization (Bozoyan, Khlgatyan, & Saghatelian, 2012; Peretto, Giachino, Aimar, Fasolo, & Bonfanti, 2005). Astrocytes are positioned at the border of the RMS during early postnatal development, following which they are transferred to the inside of the RMS (Bozoyan et al., 2012; Peretto et al., 2005). Similarly, blood vessels are transferred from the border of the RMS to the inside of the RMS during postnatal development (Bozoyan et al., 2012). During late postnatal development, the chains of immature neurons are formed within the RMS (Peretto et al., 2005). In the adult RMS, these chain-forming immature neurons utilize blood vessels as a migratory scaffold (Snapyan et al., 2009; Whitman, Fan, Rela, Rodriguez-Gil, & Greer, 2009), and are surrounded by astrocytic processes termed glial tubes (Kaneko et al., 2010; Lois et al., 1996).

Recently, it has been reported that some V-SVZ-derived immature neurons migrate toward regions other than the OB in various species (Inta et al., 2008; Le Magueresse et al., 2012; Sanai et al., 2011). For example, a pathway branching from the

RMS to the ventromedial prefrontal cortex has been observed in the infant human brain (Sanai et al., 2011). In the juvenile mouse, immature neurons have been observed migrating along blood vessels to the cerebral cortex (Inta et al., 2008; Le Magueresse et al., 2012). However, little research has been conducted to better understand these immature neurons.

In the past decade, progress in optical clearing techniques has dramatically advanced three-dimensional (3D) imaging, which is used for morphological analysis of the fixed whole brain (Chung et al., 2013; Hama et al., 2015; Hama et al., 2011; Ke, Fujimoto, & Imai, 2013; Kuwajima et al., 2013; Susaki et al., 2014). In addition, we have previously proposed a simple and rapid optical clearing protocol using 2,2'-thiodiethanol (TDE) solutions (Aoyagi, Kawakami, Osanai, Hibi, & Nemoto, 2015). Moreover, two-photon microscopy has often been used in studies of neurogenesis (Inada et al., 2011; Mizrahi, 2007; Mizrahi, Lu, Irving, Feng, & Katz, 2006; Nam et al., 2007; Sawada et al., 2011). Along with these advancements in bioimaging techniques, the generation of gigabyte- and terabyte-sized large-volume image datasets of complex information, including cell morphology and brain tissue structures, have become more frequent. However, these advancements have resulted in significant difficulties in manually processing the images and extracting their

information. Thus, the establishment of computational approaches for automatic image processing and analysis are desirable (Meijering, Carpenter, Peng, Hamprecht, & Olivo-Marin, 2016; Peng, 2008).

In this study, we utilized transgenic mice expressing enhanced green fluorescent protein (EGFP) under the control of the doublecortin (*Dcx*) promoter (*Dcx-EGFP*). By utilizing a combined protocol of TDE solutions and two-photon microscopy, the entire structure of the RMS and its surroundings in *Dcx-EGFP* mice were visualized in 3D. We also describe the spatial distribution of EGFP-positive cells and their leading process orientations, which was achieved by using computational methods based on morphological image processing. Our results demonstrated that numerous EGFP-positive cells in the areas surrounding the RMS were distributed heterogeneously, of which the leading processes were extended in various directions, suggesting that a subset of immature neurons may be detached from the RMS and migrate in various directions.

2. Materials and Methods

2.1 Animals

For immunohistochemical experiments, wild-type ICR mice of various ages (postnatal day (P) 11, P16, P29–P31, and P55–P57) were purchased from Sankyo Labo Service Corporation (Tokyo, Japan). To observe the fixed brain blocks by TDE treatment, juvenile (P15) and adult (3 months of age) transgenic mice expressing EGFP under the control of the *Dcx* promoter (*Dcx-EGFP*) were used. The *Dcx-EGFP* mouse line was originally generated by the GENSAT bacterial artificial chromosome transgenic project (Gong et al., 2003). All protocols were approved by the Institutional Animal Care and Use Committee of National University Corporation Hokkaido University (Permit Number: 10-0119). All experiments were performed in accordance with the Guidelines for the Care and Use of Laboratory Animals of the Animal Research Committee of Hokkaido University.

2.2 Immunohistochemistry

Wild-type ICR mice were anesthetized with sodium pentobarbital and transcardially perfused with phosphate buffered saline (PBS), followed by 4% paraformaldehyde in PBS. Brains were then removed and post-fixed overnight in the same fixative. After fixation, the thin fixed coronal brain slices (50 μm in thickness) were prepared by using a vibratome (7000smz; Campden Instruments Ltd, Leicestershire, UK). The fixed brain

slices were then incubated in blocking solution (10% normal donkey serum in PBS containing 0.2% Triton X-100) for 30 min at room temperature, followed by incubation with primary antibodies (see next section) overnight at 4 °C. After washing with 0.05% Tween 20 in PBS, the brain slices were incubated for 2–3 hours at room temperature with Alexa Fluor-conjugated secondary antibodies (1:500; Thermo Fisher Scientific, Waltham, MA, USA): Alexa Fluor 488 donkey anti-rabbit IgG (A-21206; RRID: AB_141708), Alexa Fluor 594 donkey anti-rabbit IgG (A-21207; RRID: AB_141637), Alexa Fluor 488 donkey anti-mouse IgG (A-21202; RRID: AB_141607), and Alexa Fluor 594 donkey anti-mouse IgG (A-21203; RRID: AB_141633).

2.3 Antibody characterization

All antibodies used for immunohistochemistry experiments were commercially available and demonstrated the appropriate pattern of cellular morphology and distribution (Bordiuk, Smith, Morin, & Semenov, 2014; Brunne et al., 2010; Hirota et al., 2012; Murata et al., 2012; Y. Wang et al., 2011). Details of the primary antibody are described in Table 1.

2.4 Preparation of fixed brains blocks and TDE treatment

Juvenile *Dcx-EGFP* mice were anesthetized with sodium pentobarbital and injected with 100 μ L (10 mg/mL) of Texas Red-conjugated dextran (70,000 MW, lysine fixable; Thermo Fisher Scientific, Waltham, MA, USA) into the tail vein to label blood vessels. Brains were then quickly removed and fixed by immersion in 4% paraformaldehyde in PBS for 3 days. Adult *Dcx-EGFP* mouse was also anesthetized with sodium pentobarbital and transcardially perfused with PBS, followed by 4% paraformaldehyde in PBS. Brain was then removed and post-fixed in the same fixative for 3 days. From these fixed brains, fixed brain blocks (500 or 800 μ m in thickness) were prepared by using a vibratome (see Section 2.2). To render the fixed brain blocks optically transparent, TDE treatment was performed based on the previously reported method (Aoyagi et al., 2015). In this study, 30% and 40% TDE solutions were prepared by mixing TDE with 10 \times PBS in a measuring cylinder, followed by dilution with Milli-Q water to achieve the final concentration. Fixed brain blocks were then immersed in a 30% TDE solution for 1 day, followed by immersion in a 40% TDE solution for 1 day.

2.5 Image acquisition

All image stacks were acquired with a confocal and two-photon microscope system (A1R-MP and FN1; Nikon, Tokyo, Japan) equipped with a Ti:sapphire laser (MaiTai

eHP DeepSee; SpectraPhysics, Santa Clara, CA, USA). To observe fixed brain slices after immunohistochemical staining, a 4× air-immersion objective lens (CFI S Fluor, numerical aperture [NA]: 0.2, working distance [WD]: 15.5 mm; Nikon, Tokyo, Japan), a 25× water-immersion objective lens (CFI Apo LWD, NA: 1.1, WD: 2 mm; Nikon), and a 25× multi-immersion objective lens (XLPLN 25×SVMP, NA: 1.0, WD: 4 mm; Olympus, Tokyo, Japan) were used. The excitation wavelengths were 488 nm and 561 nm. To observe fixed brain blocks cleared by TDE treatment, cleared brain blocks were mounted in a 40% TDE solution using iSpacer imaging chambers (SunJin Lab, Hsinchu, Taiwan) or superglued using instant glue (Aron Alpha; Toagosei, Tokyo, Japan) to the bottom of a culture dish that was subsequently filled with a 40% TDE solution. They were then placed under an objective lens of the microscope. The 4× air-immersion objective and the 25× multi-immersion objective lenses were used. The excitation wavelength was 960 nm. The emitted fluorescence signals were split with 560-nm dichroic mirrors. To obtain larger and more detailed images, including the entire structure of the RMS, 11 image stacks along the RMS were acquired and stitched together.

2.6 Analysis of the 3D distribution of EGFP-positive cells in the areas surrounding

the RMS

First, to analyze the 3D distribution of EGFP-positive cells in the areas surrounding the RMS, the 3D structure of the RMS was first identified and segmented from two-photon microscopy image stacks. The segmentation process is briefly described as follows:

- (1) The acquired image data were smoothed with a median filter to remove noise and small structures other than the RMS structure.
- (2) Smoothed images were binarized via an automatic thresholding method (the Otsu's method [(Otsu, 1979)]).
- (3) Binarized residual noise was removed using a median filter.
- (4) Holes within the RMS region were filled, and the outer shape of the RMS was smoothed via a morphological closing operation.

Second, the locations of EGFP-positive cells in the areas surrounding the RMS were detected by a pattern-matching approach. Specifically, we employed the template-matching method (Gonzalez & Woods, 2006). Using this method, a reference image of the EGFP-positive cell, which serves as a template, is generated, and the template is searched within the two-photon microscopy image to find regions that are very similar to itself. The location of the detected region is then defined as the location

of the EGFP-positive cell. In this study, we used two types of templates with parallel and perpendicular orientations of the cell. The steps of the template-matching procedure are described as follows:

(1) To generate templates, single EGFP-positive cell (expressed as Dcx) images were manually identified from micrographs.

(2) The identified images were classified into two groups: cells whose leading processes extended parallel (20 cells) or perpendicular (15 cells) to the focal plane of the objective lens.

(3) The images in each group were aligned using an affine transformation (in-plane shift and rotation). Results were then averaged, and the entire process was iteratively carried out. The averaged images were then defined as the templates.

(4) The template from the “parallel view” group was rotated in 30° intervals, from 0° to 360°. Thus, 12 templates were generated in this view to match the EGFP-positive cells, which demonstrated various orientations in the plane.

(5) Template matching based on the normalized cross-correlation coefficient was performed, and locations with higher correlation values in the correlation map were selected as the detected regions that were similar to the template. Threshold values of the cross-correlation were 0.86 for the parallel view and 0.80 for the perpendicular view.

(6). The resulting correlation maps for all templates (i.e., the 12 parallel-view templates and the single perpendicular-view template) were combined, and the positions of the EGFP-positive cells were determined. This template-matching method was performed two-dimensionally in a slice-by-slice manner. As the EGFP-positive cell is depicted in a 3D volume as a stack of consecutive slices, regions that were similar to the template were found in multiple slices in a single EGFP-positive cell volume. Thus, to obtain the 3D position of the EGFP-positive cell, the centroid of the 3D EGFP-positive cell was calculated.

Finally, the spatial distribution of EGFP-positive cells located within a 200- μm distance from the surface of the RMS was analyzed. To analyze this distribution, the 3D structure of the RMS was dilated by 200 voxels (where a voxel size is 1 μm^3), and the 3D centroid positions of the EGFP-positive cells located within this space were extracted.

All image processing procedures were performed in a Windows 7 environment (Intel $\text{\textcircled{R}}$ Xeon $\text{\textcircled{R}}$ CPU E5-1650 v3 @ 3.50 GHz and 64.0 GB RAM).

2.7 Analysis of blood vessels in the areas surrounding the RMS

First, to analyze the blood vessels surrounding the RMS, the 3D structures of the blood

vessels were first identified and segmented from two-photon microscopy image stacks.

The segmentation process is briefly described as follows:

- (1) The acquired image data were smoothed with a Gaussian filter to remove noise.
- (2) Smoothed images were binarized via an automatic thresholding method (the triangle thresholding method [(Zack, Rogers, & Latt, 1977)]).
- (3) Binarized residual noise was removed by a 3D morphological opening.

Second, we analyzed the 3D structures surrounding the blood vessels, and identified the EGFP-positive cells. The 3D structures were located at distances of 0, 2, and 12 μm from the surface of the blood vessels, and their thickness was 2 μm . Finally, we manually determined if the EGFP-positive cells formed an obvious swelling in their leading process.

2.8 Analysis of EGFP-positive cell leading process orientation

First, structures of the cell body and the whole cell of individual EGFP-positive cells were separately extracted from two-photon microscopy image stacks. The segmentation process is briefly described as follows:

- (1) The acquired image data were smoothed with a Gaussian filter to remove noise.

(2) Smoothed images were binarized via an automatic local thresholding method (the Phansalkar method [(Phansalkar, More, Sabale, & Joshi, 2011)]).

(3) To extract the structures of the cell body, fine structures, including the leading processes, were removed from binarized images by a 3D morphological opening. The remaining objects were then defined as the cell bodies of the EGFP-positive cells.

(4) To separate adjacent cells into individual cells, the marker-controlled 3D watershed segmentation method (Meyer & Beucher, 1990; Najman & Talbot, 2010) was adopted. The extracted cell body was then used as a marker for the watershed. Each segmented object was defined as the whole cell.

To then analyze only the putative migratory cells, the EGFP-positive cells that clearly were forming a swelling in their leading process were manually selected from the extracted EGFP-positive cells. The direction from the centroid of the cell body to the centroid of the whole cell was then three-dimensionally calculated as the direction of their leading process.

3. Results

3.1 Development-related changes in the distribution of Dcx-positive cells

To describe the spatial distribution of immature neurons during postnatal development, coronal brain slices (50 μm) were prepared from wild-type mice at different postnatal developmental stages (P11, P16, P29–P31, and adult), followed by staining for Dcx, a marker of immature neurons. Throughout all the developmental stages, RMS regions were identified by a high density of Dcx-positive cells, although the border of the RMS was not sharply demarcated at P11 (Figure 1). As previously described (Bozoyan et al., 2012; Peretto et al., 2005), the width of the RMS became narrower as development proceeded (Figure 1a–d). Noticeably, from P16 to P29–P31, several Dcx-positive cells were found to reside not only within the RMS but also in the areas surrounding the RMS (Figure 1f, g). These cells were observed as individual cells and their distribution seemed to be substantially biased toward the lateral region. In the adult mouse, Dcx-positive cells in the areas surrounding the RMS were remarkably decreased (Figure 1h). In the juvenile mouse, we found many Dcx-positive cells residing in the areas surrounding the RMS.

To identify astrocytes, the expression of glial fibrillary acidic protein (GFAP) was examined by immunohistochemistry. As previously described (Bozoyan et al., 2012; Peretto et al., 2005), astrocytes strongly expressing GFAP were found in the areas

surrounding the RMS at early developmental stages and within the adult RMS (Figure 1a–d, i–p). From P16 to P29–P31, the distribution of GFAP-positive astrocytes appeared different between the lateral and medial regions of the RMS (Figure 1b, c, j, k). In the medial region, astrocytes were localized outside the RMS, whereas astrocytes in the lateral region were localized to the border of the RMS at P16 and within the RMS at P29–P31. Collectively, these observations suggest a heterogeneous distribution of Dcx-positive cells surrounding the RMS in the juvenile mouse, which may be related to postnatal events involving GFAP-positive astrocytes, such as the formation of glial tubes.

3.2 Confirmation of the identity of EGFP-positive cells in the areas surrounding the RMS in juvenile *Dcx-EGFP* mice

To observe Dcx-positive cells surrounding the RMS in juvenile mice, we used *Dcx-EGFP* transgenic mouse, in which immature neurons express EGFP in the RMS (Gong et al., 2003). To confirm the identity of EGFP-positive cells in juvenile *Dcx-EGFP* mice, coronal brain slices from juvenile *Dcx-EGFP* mice (P15) were stained for GFP, Dcx, and NeuN (a marker of mature neurons). Our findings demonstrated that, in and around the RMS, EGFP-positive cells were primarily co-expressed with Dcx

(Figure 2a–c). In addition, several EGFP-positive cells were observed in the areas surrounding the RMS. These cells exhibited variability in size and EGFP fluorescence intensity (Figure 2a–i), with smaller EGFP-positive cells (7.1–11.4 μm in diameter) displaying intense EGFP fluorescence. These smaller cells also expressed Dcx at higher levels and did not express NeuN (Figure 2d–n). In contrast, larger EGFP-positive cells (12.3–17.6 μm in diameter) displayed weak EGFP fluorescence and did not express Dcx, but they did express NeuN at higher levels (Figure 2d–n), suggesting that these larger cells would be mature neurons, in which almost all of the EGFP had already been degraded during neuronal maturation. These results are consistent with a previous report indicating that GFP fluorescence intensity reflects the level of Dcx expression (Walker, Yasuda, Adams, & Bartlett, 2007). The distribution pattern of EGFP-positive cells surrounding the RMS in *Dcx-EGFP* mice was similar to that of Dcx-positive cells surrounding the RMS in wild-type mice, as shown in Figure 1. In the lateral outer region of the RMS, many EGFP-positive cells were found (Figure 2d–f), whereas few EGFP-positive cells were observed in the medial outer region of the RMS. Thus, the medial border of the RMS was sharply demarcated (Figure 2g–i). Our results suggested that Dcx-positive cells surrounding the RMS may be observed by using juvenile *Dcx-EGFP* mice.

3.3 3D visualization of the entire structure of the RMS and its surroundings in the juvenile mouse

To three-dimensionally visualize the RMS and its surroundings in the juvenile *Dcx-EGFP* mouse, we used an optical clearing protocol using TDE solutions (Aoyagi et al., 2015). According to this protocol, fixed thick brain blocks (800 μm) from juvenile *Dcx-EGFP* mice (P15) were rendered optically transparent after the mice were injected with a fixable fluorescent dextran into the tail vein to label the blood vessels. The transparent thick brain blocks were then further evaluated by two-photon microscopy. As a result, the 3D reconstruction of the entire structure of the RMS was achieved, starting from the V-SVZ and ending at the OB with blood vessels (Figure 3a, Supporting Information Movie 1). This wide-field, high-definition image consisted of $1621 \times 1572 \times 821$ pixels (0.90 $\mu\text{m}/\text{pixel}$), with a large data size (7.79 gigabytes).

From this large-scale image, we observed numerous EGFP-positive cells in the areas surrounding the RMS, with a primary location of the cells in the lateral outer region at the elbow between the vertical and horizontal limbs of the RMS (Figure 3b, d). Whereas EGFP-positive cells were packed in the inside of the RMS (Figure 3c), almost all the EGFP-positive cells surrounding the RMS were isolated as single cells or short

chains. In addition, in the areas surrounding the RMS, a large number of EGFP-positive cells displayed an elongated cell body with leading processes extended in various directions, including the direction opposite to the RMS (Figure 3e–g). Most of these cells did not appear to form an obvious swelling in their leading process, suggesting that they had already terminated their migration. Meanwhile, a small number of EGFP-positive cells displayed a shape similar to that of a mature neuron (Figure 3h). In addition, the cleared thick coronal brain block (500 μ m) from the adult *Dcx-EGFP* mouse (3 months of age) showed a decreased number of EGFP-positive cells in the areas surrounding the RMS, compared with the juvenile *Dcx-EGFP* mouse (Figure 3i–k).

Next, we examined the spatial relationship between blood vessels and EGFP-positive cells. Blood vessels were barely located within the RMS, and most were located at the outer border of the RMS, as previously reported (Bozoyan et al., 2012). Particularly, in the medial outer region of the RMS, several isolated chains of EGFP-positive cells were aligned along the blood vessels (Figure 3b). In addition, we observed that several of the EGFP-positive cells in the areas surrounding the RMS extended their leading process in the direction along the blood vessel (Figure 3f) or across the blood vessel (Figure 3g).

3.4 Spatial distribution of EGFP-positive cells in the areas surrounding the RMS

To more objectively and comprehensively identify the positions of EGFP-positive cells from the acquired wide-field and high-definition image, we established a computational method based on the template-matching method (Gonzalez & Woods, 2006). First, we developed two types of template images for identifying EGFP-positive cells that extended their leading process in various directions (for details see Materials and Methods). The first was the averaged image of 20 EGFP-positive cells expressing Dcx whose leading processes extended parallel to the focal plane of the objective lens (Figure 4a, b). The other was the averaged image of 15 EGFP-positive cells expressing Dcx whose leading processes extended perpendicular to the focal plane (Figure 4c, d). The detection accuracy and precision of Dcx-positive cells with this template-matching method was then further evaluated. To this end, three images of fixed brain slices stained for GFP and Dcx were prepared. We checked the identified cells in the areas surrounding the RMS using three parameters: True Positive (TP), False Positive (FP), and False Negative (FN). TP represented the number of cells that were identified by the method and expressed Dcx. FP represented the number of cells that were identified incorrectly by the method but did not express Dcx. FN represented the number of cells

that were not identified by the method despite expressing Dcx. The detected cells were primarily classified as TP, and the calculated accuracy reached 84% on average (Table 2). These results confirmed that our proposed method enabled the detection of Dcx-positive cells, regardless of a swelling (for details see Figure 7a), with sufficient accuracy for precise distribution analyzes. Therefore, this computational method was then applied to the large-scale image shown in Figure 3a and was used to successfully identify the positions of 7,284 EGFP-positive cells (Figure 4e, Supporting Information Movie 2).

To quantitatively analyze the cell dataset identified above and identify the detailed spatial distribution of EGFP-positive cells in the areas surrounding the RMS, we examined 3,560 EGFP-positive cells within 200 μm from the surface of the RMS. The positions of these individual EGFP-positive cells (i.e., the calculated centroid positions) were examined every 50 μm from the surface of the RMS (Figure 5a). EGFP-positive cell density decreased as the distance from the RMS increased (Figure 5b; from 20.8 cells/ $1.0 \times 10^6 \mu\text{m}^3$ to 2.8 cells/ $1.0 \times 10^6 \mu\text{m}^3$). We also visualized the distribution of EGFP-positive cells using heat maps where color was used to represent the density of EGFP-positive cells. The positions of individual EGFP-positive cells were determined by using the angle θ and the distance z , as shown in Figure 5c. Overall,

the distribution of EGFP-positive cells was extremely heterogeneous in the areas surrounding the entire RMS (Figure 5d). Interestingly, within 50 μm from the surface of the RMS, the distribution pattern of EGFP-positive cells was markedly different between the anterior and posterior regions to the elbow of the RMS (Figure 5e). In the anterior region, EGFP-positive cells were primarily localized to the lateral outer region of the RMS, whereas in the posterior region, they were primarily localized to the medial outer region of the RMS (Figure 5e). In addition, although the overall number of EGFP-positive cells decreased as the distance from the RMS increased, EGFP-positive cells were widely distributed around the elbow of the RMS (Figure 5d–h).

Furthermore, our results indicated that the distribution patterns of EGFP-positive cells were dependent on the region along the RMS. In the most posterior region close to the V-SVZ, the distribution of EGFP-positive cells was biased toward the medial region (Figure 6a–c). In contrast, in the region close to the elbow of the RMS, the distribution of EGFP-positive cells was biased toward the lateral region (Figure 6a, d, e). Similarly, in the most anterior region close to the OB, the distribution of EGFP-positive cells was also biased toward the lateral region, although the number of EGFP-positive cells was lower than that in the other regions (Figure 6a, f, g). Our 3D image analysis confirmed the heterogeneous distribution of EGFP-positive cells in the areas surrounding the RMS,

suggesting the existence of a region where immature neurons are detached from the RMS.

3.5 EGFP-positive cells and blood vessels in the areas surrounding the RMS

To obtain the population size for estimating statistical significance, we analyzed EGFP-positive cells in the lateral anterior (LA) region surrounding the RMS, where the density of EGFP-positive cells was high ($11.8 \text{ cells}/1.0 \times 10^6 \mu\text{m}^3$). Since migrating immature neurons have been shown to form a swelling in their leading process (Bellion et al., 2005; Schaar & McConnell, 2005), we first manually selected EGFP-positive cells that clearly had formed a swelling. Then, we investigated the proportion of such EGFP-positive cells against the distance from the closest blood vessel by using the computational method we developed (for details see Materials and Methods). This proportion tended to be high in the regions close to blood vessels (Figure 7a). The percentages of EGFP-positive cells that clearly had formed a swelling in each region at a distance of 0–2, 2–4, and 12–14 μm from blood vessels were 33.3% (6/18 cells), 28.2% (11/39 cells), and 18.4% (14/76 cells), respectively, suggesting that more EGFP-positive cells migrate in the regions close to blood vessels. Surely, some of the EGFP-positive cells without the swelling could be still migrating because the swelling

was not formed for the entire period of their migration (Bellion et al., 2005; Schaar & McConnell, 2005).

3.6 Orientations of the leading processes of EGFP-positive cells

Finally, we investigated the migration direction of EGFP-positive cells in the LA region. Since immature neurons migrate in the direction of their leading processes, we inferred the migration direction of EGFP-positive cells from the orientation of the leading process. It was difficult to precisely extract and trace the leading process of individual EGFP-positive cells near the RMS due to their high frequency. Therefore, we analyzed the EGFP-positive cells located approximately 50–200 μm from the surface of the RMS. Furthermore, to analyze only migrating cells, we selected EGFP-positive cells that clearly had formed a swelling. The orientation of their leading process was then calculated from the direction of the centroid of the cell body region to that of the whole cell region (Figure 7b–d, for details see Materials and Methods). The direction was classified into six groups: toward OB (OB), toward V-SVZ (SVZ), clockwise direction (CW; lateral to dorsal), counterclockwise direction (CCW; lateral to ventral), outward direction of the RMS (OR), and inward direction of the RMS (IR) (Figure 7e, f). In the region close to the elbow of the RMS, the leading processes extended in six directions

almost equally (Figure 7g–i; OB: 19.4%; SVZ: 19.4%; CW: 13.9%; CCW: 19.4%; OR: 13.9%; IR: 13.9%). In contrast, in the region close to the OB, the majority of the leading processes extended in the direction parallel to the RMS, followed in order by the OR and the CW (Figure 7j–l; OB: 33.3%; SVZ: 43.6%; CW: 2.6%; OR: 20.5%). These results indicated that immature neurons close to the elbow of the RMS may migrate in various directions, whereas those close to the OB may migrate primarily in the direction parallel to the RMS.

4. Discussion

4.1 3D imaging techniques and computational image processing methods

Although the prominent structures formed by immature neurons, particularly the RMS, have attracted much attention, the areas surrounding the RMS have not been sufficiently studied. In this study, we successfully investigated the detailed features of these putative immature neurons in the areas surrounding the RMS. To this end, we used 3D imaging techniques and computational image processing methods. The combination of the optical clearing protocol using TDE solutions and two-photon microscopy enabled the 3D reconstruction of the entire RMS and the visualization of numerous EGFP-positive

cells in the surrounding areas. Indeed, in the adult mouse, Dcx-positive cells were hardly found in the areas surrounding the RMS within the thin brain slices (Figure 1d, h); however, EGFP-positive cells were substantially observed within the thick brain block after TDE treatment (Figure 3i–k). In addition, the computational image processing protocol proposed here was primarily composed of morphological image processing (Kimori, 2011; Kimori, Hikino, Nishimura, & Mano, 2016) and served to achieve the automatic segmentation of EGFP-positive cells, blood vessels, and the RMS region. In particular, the computational image processing protocol based on the template-matching method enabled the identification of the positions of numerous EGFP-positive cells and their spatial distribution. If these analyzes were performed manually, considerable effort and time would be necessary.

4.2 EGFP-positive cells in the areas surrounding the RMS

In general, V-SVZ-derived immature neurons are believed to migrate toward the OB through the RMS. However, in this study, we successfully demonstrated that numerous EGFP-positive cells were localized to the areas surrounding the RMS in juvenile mice. A large portion of the EGFP-positive cells were determined to be Dcx-positive cells (Figure 2), with 20%–30% clearly forming a swelling, while the remainder did not

(Figure 7a). The majority of the EGFP-positive cells identified in Figures 5 and 6 were Dcx-positive cells, as our template-matching method for distribution analysis detected Dcx-positive cells with an average accuracy of 84% (Table 2). When analyzing the direction of migration (Figure 7g–l), we targeted only the group of EGFP-positive cells that had clearly formed a swelling (i.e., cells with migratory morphology). Conversely, our template-matching method also identified the EGFP-positive cells with more complex morphology (e.g., the cell shown in Figure 3h). These cells are morphologically similar to small axonless neurons, neocortical interneurons generated in the postnatal V-SVZ (Le Magueresse et al., 2011). To analyze the distribution of these cells, the computational image processing protocol proposed in this study needs to be further improved. Note that our experiments in this study did not directly visualize cell migration in succession under living conditions; thus, some of the EGFP-positive cells may have transiently lost their swellings during migration (Bellion et al., 2005; Schaar & McConnell, 2005).

We cannot, nonetheless, exclude the possibility that the EGFP-positive cells identified in this study represented only cells that had already terminated their migration during embryonic development. However, it is also likely that they represented cells that were migrating directly from the RMS during postnatal development, simply

because of their distribution near the RMS (Figure 5b). Indeed, it has been reported that in several species, including mouse, a portion of the immature neurons is detached from the RMS (De Marchis, Fasolo, & Puche, 2004; Martin, Katzenelson, Koehler, & Chang, 2013; Nam et al., 2007; Sanai et al., 2011; Shapiro et al., 2007).

4.3 Migration of EGFP-positive cells in the areas surrounding the RMS

The 3D visualization of individual EGFP-positive cells also allowed for the 3D analysis of such fine structures as the leading processes of these cells. When using conventional 2D imaging methods, it is difficult to trace the long and fine leading process of cells extending three-dimensionally within the brain. From the orientation of the leading processes, we inferred the direction of EGFP-positive cell migration and found that the orientation patterns differed depending on their locations (Figure 7g–l). In the region close to the elbow of the RMS, EGFP-positive cells extended their leading processes almost uniformly (Figure 7g–i), suggesting that they may migrate in various directions. In contrast, in the region close to the OB, the majority of the EGFP-positive cells extended their leading processes in the direction parallel to the RMS (Figure 7j–l), suggesting that they may migrate in parallel with immature neurons within the RMS. The leading processes in this region also extended to the OR (Figure 7j–l), which

supports the hypothesis that immature neurons surrounding the RMS may migrate from the RMS.

In the areas surrounding the RMS, a portion of the EGFP-positive cells were observed to be adjacent to blood vessels (Figure 3b, f). In this regard, these cells may utilize the blood vessel as a migratory scaffold, as do immature neurons in other regions (Bovetti et al., 2007; Le Magueresse et al., 2012; Snapyan et al., 2009; Whitman et al., 2009). However, our results also demonstrated that the EGFP-positive cells that did not align along the blood vessels (Figure 3e, g) may instead migrate along other structures such as astrocytes or axons.

4.4 Postnatal development of the RMS and its surroundings

As previously reported (Bozoyan et al., 2012; Peretto et al., 2005), we observed that the RMS and its surroundings undergo a structural reorganization during the first three postnatal weeks (Figure 1). Notably, many Dcx-positive cells were localized to the areas surrounding the RMS in the juvenile mouse, and the width of the RMS was narrowed in the adult mouse. If the Dcx-positive cells surrounding the RMS migrate from the RMS, as discussed above, then this may result in a decreasing number of immature neurons within the RMS, thus narrowing its width.

The appearance of Dcx-positive cells in the areas surrounding the RMS coincided with the appearance of GFAP-positive astrocytes within the RMS (Figure 1m–p). Thus, the appearance of Dcx-positive cells may be linked to postnatal events involving GFAP-positive astrocytes, such as the formation of glial tubes, although this formation has been reported to occur from the medial side of the RMS (Peretto et al., 2005). Indeed, many EGFP-positive cells were found around the elbow of the RMS (Figure 5d–h), where GFAP-positive astrocytes have been reported to increase (Law, Pencea, Buck, & Luskin, 1999). Conversely, some extracellular diffusible factors might be involved in the appearance and migration of the Dcx-positive cells during postnatal development. The migration of immature neurons within the RMS has been shown to be regulated by a variety of factors, including chemoattractants for immature neurons (e.g., Netrin-1, brain-derived neurotrophic factor, and hepatocyte growth factor; Chiaramello et al., 2007; Murase & Horwitz, 2002; Wang, Zhang, Gyetko, & Parent, 2011) and chemorepellents for immature neurons, such as Slit2 (Sawamoto et al., 2006; Wu et al., 1999).

Glial tubes have often been considered as a physical barrier between the RMS and its surrounding areas (Lois et al., 1996). The remarkable decrease in Dcx-positive cells surrounding the RMS in the adult brain (Figures 1d and h and 3i–k) may actually result

from complete glial tubes preventing immature neurons from detaching from the RMS.

4.5 Conclusion and future applications

In conclusion, *Dcx*-expressing cells in juvenile mice were found to be distributed heterogeneously in the areas surrounding the RMS, and the orientation patterns of their leading processes differed depending on their locations (Figure 8). This detailed description was successfully obtained through a combination of 3D imaging techniques and the computational image processing protocol developed here. This methodology can be applied to various experimental designs for further studies of immature neurons. For example, when applied to *GAD-EGFP* transgenic mouse where only a subset of immature neurons is labeled (Nam et al., 2007), the migratory directions of immature neurons within the RMS can be examined in 3D.

As described above, our analyzes using fixed brains cannot conclusively determine whether the EGFP-positive cells examined here migrated from the RMS during postnatal development or have remained stationary since embryonic development. In addition, these cells were primarily present not as chains but as individual cells, suggesting that they may exhibit different migratory behavior from immature neurons within the RMS. To determine their origin and migratory behavior,

EGFP-positive cells in the area surrounding the RMS should be observed directly *in vivo*. Recently, we proposed an *in vivo* imaging technique for visualizing neurons in deeper regions, including the dentate gyrus of the hippocampus in a living mouse brain (Kawakami et al., 2013). Since the RMS also exists in deeper regions, we intend to advance such *in vivo* imaging techniques for observing the RMS and its surroundings in a living mouse in future studies.

Lastly, the methodology developed here may also be applicable to various disease and injury models, which allows for the analysis of immature neurons migrating toward damaged regions. Indeed, immature neurons derived from the V-SVZ have been investigated as a therapeutic target for various neurological disorders (Kaneko, Sawada, & Sawamoto, 2017; Lu, Manaenko, & Hu, 2017; Ruan et al., 2014). Conversely, our results suggested that numerous immature neurons surrounding the RMS in the juvenile mouse migrate in various directions. Therefore, although the number of the cells surrounding the RMS in the adult brain was decreased (Figures 1d and h and 3i–k), targeting these immature neurons can enhance migration toward damaged regions. In addition, for the development of such a therapy, it might be necessary to investigate the EGFP-positive cells surrounding the RMS after a brain injury. Overall, our novel findings provide morphological information of Dcx-expressing cells in the areas

surrounding the RMS, and our methodology should provide further important information about immature neurons involved in physiological processes, as well as pathological conditions.

References

- Anton, E. S., Ghashghaei, H. T., Weber, J. L., McCann, C., Fischer, T. M., Cheung, I. D., . . . Lai, C. (2004). Receptor tyrosine kinase ErbB4 modulates neuroblast migration and placement in the adult forebrain. *Nature Neuroscience*, *7*, 1319–1328. doi:10.1038/nm1345
- Aoyagi, Y., Kawakami, R., Osanai, H., Hibi, T., & Nemoto, T. (2015). A rapid optical clearing protocol using 2,2'-thiodiethanol for microscopic observation of fixed mouse brain. *PLoS One*, *10*, e0116280. doi:10.1371/journal.pone.0116280
- Arvidsson, A., Collin, T., Kirik, D., Kokaia, Z., & Lindvall, O. (2002). Neuronal replacement from endogenous precursors in the adult brain after stroke. *Nature Medicine*, *8*, 963–970. doi:10.1038/nm747
- Bellion, A., Baudoin, J. P., Alvarez, C., Bornens, M., & Métin, C. (2005). Nucleokinesis in tangentially migrating neurons comprises two alternating phases: forward migration of the Golgi/centrosome associated with centrosome splitting and myosin contraction at the rear. *Journal of Neuroscience*, *25*, 5691–5699. doi:10.1523/JNEUROSCI.1030-05.2005
- Bordiuk, O. L., Smith, K., Morin, P. J., & Semënov, M. V. (2014). Cell proliferation and neurogenesis in adult mouse brain. *PLoS One*, *9*, e111453.

doi:10.1371/journal.pone.0111453

Bovetti, S., Hsieh, Y. C., Bovolin, P., Perroteau, I., Kazunori, T., & Puche, A. C. (2007).

Blood vessels form a scaffold for neuroblast migration in the adult olfactory bulb. *Journal of Neuroscience*, *27*, 5976–5980.

doi:10.1523/JNEUROSCI.0678-07.2007

Bozoyan, L., Khlghatyan, J., & Saghatelian, A. (2012). Astrocytes control the

development of the migration-promoting vasculature scaffold in the postnatal brain via VEGF signaling. *Journal of Neuroscience*, *32*, 1687–1704.

doi:10.1523/JNEUROSCI.5531-11.2012

Brunne, B., Zhao, S., Derouiche, A., Herz, J., May, P., Frotscher, M., & Bock, H. H.

(2010). Origin, maturation, and astroglial transformation of secondary radial glial cells in the developing dentate gyrus. *Glia*, *58*, 1553–1569.

doi:10.1002/glia.21029

Chiaramello, S., Dalmaso, G., Bezin, L., Marcel, D., Jourdan, F., Peretto, P., . . . De

Marchis, S. (2007). BDNF/ TrkB interaction regulates migration of SVZ precursor cells via PI3-K and MAP-K signalling pathways. *European Journal of Neuroscience*, *26*, 1780–1790. doi:10.1111/j.1460-9568.2007.05818.x

Chung, K., Wallace, J., Kim, S. Y., Kalyanasundaram, S., Andalman, A. S., Davidson,

- T. J., . . . Deisseroth, K. (2013). Structural and molecular interrogation of intact biological systems. *Nature*, *497*, 332-337. doi:10.1038/nature12107
- De Marchis, S., Fasolo, A., & Puche, A. C. (2004). Subventricular zone-derived neuronal progenitors migrate into the subcortical forebrain of postnatal mice. *Journal of Comparative Neurology*, *476*, 290–300. doi:10.1002/cne.20217
- Fuentealba, L. C., Obernier, K., & Alvarez-Buylla, A. (2012). Adult neural stem cells bridge their niche. *Cell Stem Cell*, *10*, 698–708. doi:10.1016/j.stem.2012.05.012
- García-González, D., Khodosevich, K., Watanabe, Y., Rollenhagen, A., Lübke, J. H. R., & Monyer, H. (2017). Serotonergic projections govern postnatal neuroblast migration. *Neuron*, *94*, 534–549.e539. doi:10.1016/j.neuron.2017.04.013
- Gong, S., Zheng, C., Doughty, M. L., Losos, K., Didkovsky, N., Schambra, U. B., . . . Heintz, N. (2003). A gene expression atlas of the central nervous system based on bacterial artificial chromosomes. *Nature*, *425*, 917–925. doi:10.1038/nature02033
- Gonzalez, R. C., & Woods, R. E. (2006). Digital image processing (3rd Edition). Englewood Cliffs, NJ. Prentice-Hall, Inc.
- Hama, H., Hioki, H., Namiki, K., Hoshida, T., Kurokawa, H., Ishidate, F., . . . Miyawaki, A. (2015). ScaleS: an optical clearing palette for biological imaging.

Nature Neuroscience, 18, 1518–1529. doi:10.1038/nn.4107

Hama, H., Kurokawa, H., Kawano, H., Ando, R., Shimogori, T., Noda, H., . . .

Miyawaki, A. (2011). Scale: a chemical approach for fluorescence imaging and reconstruction of transparent mouse brain. *Nature Neuroscience*, 14, 1481–1488.

doi:10.1038/nn.2928

Hirota, Y., Sawada, M., Kida, Y. S., Huang, S. H., Yamada, O., Sakaguchi, M., . . .

Sawamoto, K. (2012). Roles of planar cell polarity signaling in maturation of neuronal precursor cells in the postnatal mouse olfactory bulb. *Stem Cells*, 30,

1726–1733. doi:10.1002/stem.1137

Inada, H., Watanabe, M., Uchida, T., Ishibashi, H., Wake, H., Nemoto, T., . . .

Nabekura, J. (2011). GABA regulates the multidirectional tangential migration of GABAergic interneurons in living neonatal mice. *PLoS One*, 6, e27048.

doi:10.1371/journal.pone.0027048

Inta, D., Alfonso, J., von Engelhardt, J., Kreuzberg, M. M., Meyer, A. H., van Hooft, J.

A., & Monyer, H. (2008). Neurogenesis and widespread forebrain migration of distinct GABAergic neurons from the postnatal subventricular zone.

Proceedings of the Natural Academy of Sciences U S A, 105, 20994–20999.

doi:10.1073/pnas.0807059105

Jinnou, H., Sawada, M., Kawase, K., Kaneko, N., Herranz-Pérez, V., Miyamoto, T., . . .

Sawamoto, K. (2018). Radial glial fibers promote neuronal migration and functional recovery after neonatal brain injury. *Cell Stem Cell*, *22*, 128–137.e129. doi:10.1016/j.stem.2017.11.005

Kaneko, N., Marín, O., Koike, M., Hirota, Y., Uchiyama, Y., Wu, J. Y., . . . Sawamoto,

K. (2010). New neurons clear the path of astrocytic processes for their rapid migration in the adult brain. *Neuron*, *67*, 213–223. doi:10.1016/j.neuron.2010.06.018

Kaneko, N., Sawada, M., & Sawamoto, K. (2017). Mechanisms of neuronal migration

in the adult brain. *Journal of Neurochemistry*, *141*, 835–847. doi:10.1111/jnc.14002

Kawakami, R., Sawada, K., Sato, A., Hibi, T., Kozawa, Y., Sato, S., . . . Nemoto, T.

(2013). Visualizing hippocampal neurons with *in vivo* two-photon microscopy using a 1030 nm picosecond pulse laser. *Scientific Reports*, *3*, 1014. doi:10.1038/srep01014

Ke, M. T., Fujimoto, S., & Imai, T. (2013). SeeDB: a simple and

morphology-preserving optical clearing agent for neuronal circuit reconstruction. *Nature Neuroscience*, *16*, 1154–1161. doi:10.1038/nn.3447

- Kimori, Y. (2011). Mathematical morphology-based approach to the enhancement of morphological features in medical images. *Journal of Clinical Bioinformatics*, *1*, 33. doi:10.1186/2043-9113-1-33
- Kimori, Y., Hikino, K., Nishimura, M., & Mano, S. (2016). Quantifying morphological features of actin cytoskeletal filaments in plant cells based on mathematical morphology. *Journal of Theoretical Biology*, *389*, 123–131. doi:10.1016/j.jtbi.2015.10.031
- Kuwajima, T., Sitko, A. A., Bhansali, P., Jurgens, C., Guido, W., & Mason, C. (2013). ClearT: a detergent- and solvent-free clearing method for neuronal and non-neuronal tissue. *Development*, *140*, 1364–1368. doi:10.1242/dev.091844
- Law, A. K., Pencea, V., Buck, C. R., & Luskin, M. B. (1999). Neurogenesis and neuronal migration in the neonatal rat forebrain anterior subventricular zone do not require GFAP-positive astrocytes. *Developmental Biology*, *216*, 622-634. doi:10.1006/dbio.1999.9498
- Le Magueresse, C., Alfonso, J., Bark, C., Eliava, M., Khrulev, S., & Monyer, H. (2012). Subventricular zone-derived neuroblasts use vasculature as a scaffold to migrate radially to the cortex in neonatal mice. *Cerebral Cortex*, *22*, 2285–2296. doi:10.1093/cercor/bhr302

- Le Magueresse, C., Alfonso, J., Khodosevich, K., Arroyo Martín, A. A., Bark, C., & Monyer, H. (2011). "Small axonless neurons": postnatally generated neocortical interneurons with delayed functional maturation. *Journal of Neuroscience*, *31*, 16731–16747. doi:10.1523/JNEUROSCI.4273-11.2011
- Lois, C., & Alvarez-Buylla, A. (1994). Long-distance neuronal migration in the adult mammalian brain. *Science*, *264*, 1145–1148.
- Lois, C., García-Verdugo, J. M., & Alvarez-Buylla, A. (1996). Chain migration of neuronal precursors. *Science*, *271*, 978–981.
- Lu, J., Manaenko, A., & Hu, Q. (2017). Targeting adult neurogenesis for poststroke therapy. *Stem Cells International*, *2017*, 5868632. doi:10.1155/2017/5868632
- Luskin, M. B. (1993). Restricted proliferation and migration of postnatally generated neurons derived from the forebrain subventricular zone. *Neuron*, *11*, 173–189.
- Martin, L. J., Katzenelson, A., Koehler, R. C., & Chang, Q. (2013). The olfactory bulb in newborn piglet is a reservoir of neural stem and progenitor cells. *PLoS One*, *8*, e81105. doi:10.1371/journal.pone.0081105
- Meijering, E., Carpenter, A. E., Peng, H., Hamprecht, F. A., & Olivo-Marin, J. C. (2016). Imagining the future of bioimage analysis. *Nature Biotechnology*, *34*, 1250–1255. doi:10.1038/nbt.3722

- Meyer, F., & Beucher, S. (1990). Morphological segmentation. *Journal of Visual Communication and Image Representation, 1*, 21–46.
doi:[https://doi.org/10.1016/1047-3203\(90\)90014-M](https://doi.org/10.1016/1047-3203(90)90014-M)
- Mizrahi, A. (2007). Dendritic development and plasticity of adult-born neurons in the mouse olfactory bulb. *Nature Neuroscience, 10*, 444–452. doi:10.1038/nn1875
- Mizrahi, A., Lu, J., Irving, R., Feng, G., & Katz, L. C. (2006). *In vivo* imaging of juxtglomerular neuron turnover in the mouse olfactory bulb. *Proceedings of the National Academy of Sciences U S A, 103*, 1912–1917.
doi:10.1073/pnas.0506297103
- Murase, S., & Horwitz, A. F. (2002). Deleted in colorectal carcinoma and differentially expressed integrins mediate the directional migration of neural precursors in the rostral migratory stream. *Journal of Neuroscience, 22*, 3568–3579. doi:20026349
- Murata, D., Nomura, K. H., Dejima, K., Mizuguchi, S., Kawasaki, N., Matsuishi-Nakajima, Y., . . . Nomura, K. (2012). GPI-anchor synthesis is indispensable for the germline development of the nematode *Caenorhabditis elegans*. *Molecular Biology of the Cell, 23*, 982–995.
doi:10.1091/mbc.E10-10-0855
- Najman, L., & Talbot, H. (Eds.). (2010). Mathematical morphology: from theory to

applications. London, UK ISTE-Wiley.

Nam, S. C., Kim, Y., Dryanovski, D., Walker, A., Goings, G., Woolfrey, K., . . . Szele, F. G. (2007). Dynamic features of postnatal subventricular zone cell motility: a two-photon time-lapse study. *Journal of Comparative Neurology*, *505*, 190–208. doi:10.1002/cne.21473

Ota, H., Hikita, T., Sawada, M., Nishioka, T., Matsumoto, M., Komura, M., . . . Sawamoto, K. (2014). Speed control for neuronal migration in the postnatal brain by Gmip-mediated local inactivation of RhoA. *Nature Communications*, *5*, 4532. doi:10.1038/ncomms5532

Otsu, N. (1979). A threshold selection method from gray-level histograms. *IEEE Transactions on Systems, Man, and Cybernetics*, *9*, 62–66. doi:10.1109/TSMC.1979.4310076

Parent, J. M., Vexler, Z. S., Gong, C., Derugin, N., & Ferriero, D. M. (2002). Rat forebrain neurogenesis and striatal neuron replacement after focal stroke. *Annals of Neurology*, *52*, 802–813. doi:10.1002/ana.10393

Peng, H. (2008). Bioimage informatics: a new area of engineering biology. *Bioinformatics*, *24*, 1827–1836. doi:10.1093/bioinformatics/btn346

Peretto, P., Giachino, C., Aimar, P., Fasolo, A., & Bonfanti, L. (2005). Chain formation

and glial tube assembly in the shift from neonatal to adult subventricular zone of the rodent forebrain. *Journal of Comparative Neurology*, 487, 407–427.

doi:10.1002/cne.20576

Phansalkar, N., More, S., Sabale, A., & Joshi, M. (2011, 10-12 Feb. 2011). Adaptive local thresholding for detection of nuclei in diversity stained cytology images. Paper presented at the 2011 International Conference on Communications and Signal Processing.

Ruan, L., Lau, B. W., Wang, J., Huang, L., Zhuge, Q., Wang, B., . . . So, K. F. (2014). Neurogenesis in neurological and psychiatric diseases and brain injury: from bench to bedside. *Progress in Neurobiology*, 115, 116–137.

doi:10.1016/j.pneurobio.2013.12.006

Sanai, N., Nguyen, T., Ihrie, R. A., Mirzadeh, Z., Tsai, H. H., Wong, M., . . .

Alvarez-Buylla, A. (2011). Corridors of migrating neurons in the human brain and their decline during infancy. *Nature*, 478, 382–386.

doi:10.1038/nature10487

Sawada, M., Kaneko, N., Inada, H., Wake, H., Kato, Y., Yanagawa, Y., . . . Sawamoto, K. (2011). Sensory input regulates spatial and subtype-specific patterns of neuronal turnover in the adult olfactory bulb. *Journal of Neuroscience*, 31,

11587–11596. doi:10.1523/JNEUROSCI.0614-11.2011

Sawada, M., Ohno, N., Kawaguchi, M., Huang, S. H., Hikita, T., Sakurai, Y., . . .

Sawamoto, K. (2018). PlexinD1 signaling controls morphological changes and migration termination in newborn neurons. *EMBO Journal*, *37*.

doi:10.15252/emj.201797404

Sawamoto, K., Wichterle, H., Gonzalez-Perez, O., Cholfin, J. A., Yamada, M., Spassky,

N., . . . Alvarez-Buylla, A. (2006). New neurons follow the flow of cerebrospinal fluid in the adult brain. *Science*, *311*, 629–632.

doi:10.1126/science.1119133

Schaar, B. T., & McConnell, S. K. (2005). Cytoskeletal coordination during neuronal

migration. *Proceedings of the National Academy of Sciences U S A*, *102*, 13652–

13657. doi:10.1073/pnas.0506008102

Shapiro, L. A., Ng, K. L., Kinyamu, R., Whitaker-Azmitia, P., Geisert, E. E.,

Blurton-Jones, M., . . . Ribak, C. E. (2007). Origin, migration and fate of newly generated neurons in the adult rodent piriform cortex. *Brain Structure and*

Function, *212*, 133–148. doi:10.1007/s00429-007-0151-3

Snapyan, M., Lemasson, M., Brill, M. S., Blais, M., Massouh, M., Ninkovic, J., . . .

Saghatelian, A. (2009). Vasculature guides migrating neuronal precursors in the

adult mammalian forebrain via brain-derived neurotrophic factor signaling.

Journal of Neuroscience, 29, 4172–4188.

doi:10.1523/JNEUROSCI.4956-08.2009

Susaki, E. A., Tainaka, K., Perrin, D., Kishino, F., Tawara, T., Watanabe, T. M., . . .

Ueda, H. R. (2014). Whole-brain imaging with single-cell resolution using chemical cocktails and computational analysis. *Cell*, 157, 726–739.

doi:10.1016/j.cell.2014.03.042

Walker, T. L., Yasuda, T., Adams, D. J., & Bartlett, P. F. (2007). The

doublecortin-expressing population in the developing and adult brain contains multipotential precursors in addition to neuronal-lineage cells. *Journal of Neuroscience*, 27, 3734–3742. doi:10.1523/JNEUROSCI.5060-06.2007

Wang, T. W., Zhang, H., Gyetko, M. R., & Parent, J. M. (2011). Hepatocyte growth

factor acts as a mitogen and chemoattractant for postnatal subventricular zone-olfactory bulb neurogenesis. *Molecular and Cellular Neuroscience*, 48,

38–50. doi:10.1016/j.mcn.2011.06.003

Wang, Y., Kaneko, N., Asai, N., Enomoto, A., Isotani-Sakakibara, M., Kato, T., . . .

Takahashi, M. (2011). Girdin is an intrinsic regulator of neuroblast chain migration in the rostral migratory stream of the postnatal brain. *Journal of*

Neuroscience, 31, 8109–8122. doi:10.1523/JNEUROSCI.1130-11.2011

Whitman, M. C., Fan, W., Rela, L., Rodriguez-Gil, D. J., & Greer, C. A. (2009). Blood vessels form a migratory scaffold in the rostral migratory stream. *Journal of Comparative Neurology*, 516, 94–104. doi:10.1002/cne.22093

Wu, W., Wong, K., Chen, J., Jiang, Z., Dupuis, S., Wu, J. Y., & Rao, Y. (1999). Directional guidance of neuronal migration in the olfactory system by the protein Slit. *Nature*, 400, 331–336. doi:10.1038/22477

Yamashita, T., Ninomiya, M., Hernández Acosta, P., García-Verdugo, J. M., Sunabori, T., Sakaguchi, M., . . . Sawamoto, K. (2006). Subventricular zone-derived neuroblasts migrate and differentiate into mature neurons in the post-stroke adult striatum. *Journal of Neuroscience*, 26, 6627–6636. doi:10.1523/JNEUROSCI.0149-06.2006

Yang, Z., Covey, M. V., Bitel, C. L., Ni, L., Jonakait, G. M., & Levison, S. W. (2007). Sustained neocortical neurogenesis after neonatal hypoxic/ischemic injury. *Annals of Neurology*, 61, 199–208. doi:10.1002/ana.21068

Zack, G. W., Rogers, W. E., & Latt, S. A. (1977). Automatic measurement of sister chromatid exchange frequency. *Journal of Histochemistry and Cytochemistry*, 25, 741–753. doi:10.1177/25.7.70454

Figure Legends

Figure 1. Development-related changes in the distribution of Dcx-positive cells and GFAP-positive astrocytes. (a–d) Images of coronal slices of the RMS stained for Dcx (green) and GFAP (magenta) in wild-type mice at P11 (a), P16 (b), P29–P31 (c), and P55–P57 (d). (e–p) Magnified images of the lateral outer regions of the RMS corresponding to the dashed boxed regions shown in (a–d). All images are maximum projection images. M, medial; L, lateral; D, dorsal; V, ventral.

Figure 2. Identity of EGFP-positive cells in the areas surrounding the RMS in the *Dcx-EGFP* mouse. (a–c) Images of coronal slices of the RMS in the *Dcx-EGFP* mouse at P15. The majority of the EGFP-positive cells (green) also exhibit expression of Dcx, a marker for immature neurons (magenta). (d–i) Magnified images of the two dashed boxed regions in (a–c): the lateral (d–f) and medial (g–i) outer regions of the RMS. The arrowheads indicate the EGFP-positive cells expressing Dcx. The dashed circles indicate the EGFP-positive cells that did not express Dcx. (j–l) Images of the lateral outer region of the RMS. The arrowheads indicate the EGFP-positive cells expressing NeuN, a marker for mature neurons. (m, n) Plots of the fluorescence intensity of Dcx (m) or NeuN (n) labeling against the fluorescence intensity of EGFP. The dashed line indicates the regression line. All images are maximum projection images.

Figure 3. 3D visualization of the entire structure of the RMS and its surroundings.

(a) 3D-reconstructed image of the entire structure of the RMS in optically transparent fixed brain block (800 μm in thickness) from the *Dcx-EGFP* mouse at P15.

EGFP-positive cells (green) and blood vessels (magenta) were observed. The large-scale image was acquired by stitching 3D image stacks (11 stacks) together. The left inset shows a low-magnification image in which the dashed box shows the magnified region.

(b–d) Maximum projection images of the medial outer region of the RMS (b), the RMS region (c), and the lateral outer region of the RMS (d) in (a). (e–h) Maximum projection images of individual EGFP-positive cells in the areas surrounding the RMS. The white dashed line indicates the border of the RMS region. These EGFP-positive cells display a shape characteristic of immature neurons (e–g) or mature neurons (h). Several of the EGFP-positive cells in the areas surrounding the RMS also extend their leading process in the direction opposite of the RMS (e), along the blood vessel (f), or across the blood vessel (g). (i) Maximum projection image of the coronal section of the RMS in the adult *Dcx-EGFP* mouse. (j, k) Magnified images of the dashed boxed regions as shown in (i).

Figure 4. Identification of the positions of EGFP-positive cells based on the

template-matching method. (a, c) Schematic drawing of the two types of template images with different views. Each illustration shows EGFP-positive cells that extend their leading process in parallel to the focal plane (parallel to the xy plane), (a) and perpendicular to the focal plane (the z -axis direction) (c). (b, d) Images of single EGFP-positive cells that express Dcx corresponding to (a, c), respectively. Note that each image in the upper left (white box) shows the template image, which is the averaged image of the EGFP-positive cells expressing Dcx, and is generated from the other images. Scale bars = 5 μm . (e) 3D map showing the positions of EGFP-positive cells in the areas surrounding the RMS. The positions of individual EGFP-positive cells were assigned random colors. The asterisk indicates the elbow of the RMS. The inset shows the magnified image of the lateral outer region at the elbow.

Figure 5. Comprehensive analysis of the spatial distribution of EGFP-positive cells in the areas surrounding the RMS. (a) Schematic drawing of the analyzed region. EGFP-positive cells within 200 μm from the surface of the RMS were analyzed every 50 μm . (b) Graph showing the density of EGFP-positive cells against the distance from the surface of RMS. (c) Schematic drawing for analyzing the position of EGFP-positive cells. The angle θ is determined by the angle of EGFP-positive cells from the dorsal

direction in the coronal section (left). The distance z is determined by the distance from the V-SVZ along the anterior–posterior axis, and the distance $400\ \mu\text{m}$ is the position corresponding to the elbow of the RMS (right). (d–h) Heat maps showing the distribution of EGFP-positive cells in the areas surrounding the RMS. The heat map color represents the density of EGFP-positive cells, and the angle θ and the distance z are defined in (c). Each map shows the distribution in the overall region ($0\text{--}200\ \mu\text{m}$) (d), and the distribution in the region within $0\text{--}50$ (e), $50\text{--}100$ (f), $100\text{--}150$ (g), and $150\text{--}200\ \mu\text{m}$ (h) from the surface of the RMS, as shown in (a). The asterisks indicate the position corresponding to the elbow of the RMS. M, medial; L, lateral; D, dorsal; V, ventral.

Figure 6. Change in distribution of EGFP-positive cells along the RMS. (a)

Schematic drawing of the sagittal section. The asterisk indicates the elbow of the RMS.

(b, d, f) Plots showing the location of EGFP-positive cells in the region corresponding to the boxed regions shown in (a). (c, e, g) Graphs showing the spatial distribution of EGFP-positive cells corresponding to (b, d, f), respectively. Each axis shows the number of EGFP-positive cells. M, medial; L, lateral; D, dorsal; V, ventral.

Figure 7. Orientations of the leading processes of EGFP-positive cells. (a) Graph

showing the percentages of EGFP-positive cells forming an obvious swelling in their leading process against the distance from the closest blood vessels. (b) 3D segmentation image of individual EGFP-positive cells in the LA region. Individual cells were assigned random colors. (c, d) Images of the cell body (b) and the whole cell (c) of the EGFP-positive cell. The brown lines represent the outlines of the cell body and whole cell regions. The orientation of the leading process was determined by the direction from the centroid of the cell body region (pink dot) to that of the whole cell region (light blue dot). (e, f) Schematic drawings for the orientation analysis of the leading process. The calculated direction was first normalized (that is, length = 1; black arrow), and three components (the parallel, the tangential, and the radial components; gray arrows) were investigated. The directions of the leading processes were classified into six groups: toward OB (OB), toward V-SVZ (SVZ), clockwise direction (CW; lateral to dorsal), counterclockwise direction (CCW; lateral to ventral), outward direction of RMS (OR), and inward direction of RMS (IR). (g, h, j, k) Plots showing the orientations of the leading processes of the EGFP-positive cells close to the elbow (g, h) and close to the OB (j, k). The axes (left and bottom) show the magnitude of individual components whose direction is indicated by the sign (positive or negative) as shown in (e, f). (i, l) Graphs showing the proportion of the EGFP-positive cells extending their leading

processes in each direction in the region close to the elbow (i) and close to the OB (l).

M, medial; L, lateral; D, dorsal; V, ventral.

Figure 8. Schematic drawing of putative immature neurons in the areas

surrounding the RMS in the juvenile mouse. In the juvenile mouse, numerous

Dcx-expressing cells were found to be distributed heterogeneously in the areas

surrounding the RMS. Their spatial distribution pattern was different between the

anterior and posterior regions of the elbow of the RMS. In the posterior region, more

Dcx-expressing cells were distributed in the medial outer region of the RMS (i),

whereas the distribution of Dcx-expressing cells in the anterior region was biased

toward the lateral outer region of the RMS (ii, iii). Noticeably, numerous

Dcx-expressing cells were localized to the lateral outer region at the elbow of the RMS

(ii). In addition, the orientation patterns of the leading processes of the Dcx-expressing

cells differed depending on their locations. The leading processes of Dcx-expressing

cells close to the elbow extended in various directions, whereas those of Dcx-expressing

cells close to the OB extended primarily in the direction parallel to the RMS. M, medial;

L, lateral; D, dorsal; V, ventral.

Tables

Table 1. Primary antibodies used for immunohistochemistry

Antigen	Description of immunogen	Manufacturing details	Working dilution
Dcx	Synthetic peptide corresponding to human Dcx	Cell Signaling Technology, rabbit polyclonal, #4604, RRID: AB_561007	1:200
GFAP	Purified GFAP from pig spinal cord	Sigma, mouse monoclonal, G3893, RRID: AB_477010	1:500
NeuN	Purified cell nuclei from mouse brain	Millipore, mouse monoclonal, MAB377, RRID: AB_2298772	1:100
GFP	Recombinant GFP	MBL International, rabbit polyclonal, 598, RRID: AB_591819	1:1000
GFP	GFP peptide	Wako Pure Chemical Industries, mouse monoclonal, 012-20461, RRID: AB_664697	1:1000

Dcx = doublecortin; GFAP = glial fibrillary acidic protein; NeuN = neuronal nuclei;

GFP = green fluorescent protein.

Table 2. Detection accuracy of Dcx-positive cells by the template-matching method

	TP	FP	FN	Accuracy (TP / (TP + FP))
Sample #1	159	23	11	0.87
Sample #2	69	15	11	0.82
Sample #3	115	23	9	0.83

TP = True Positive; FP = False Positive; FN = False Negative.

Figure 1

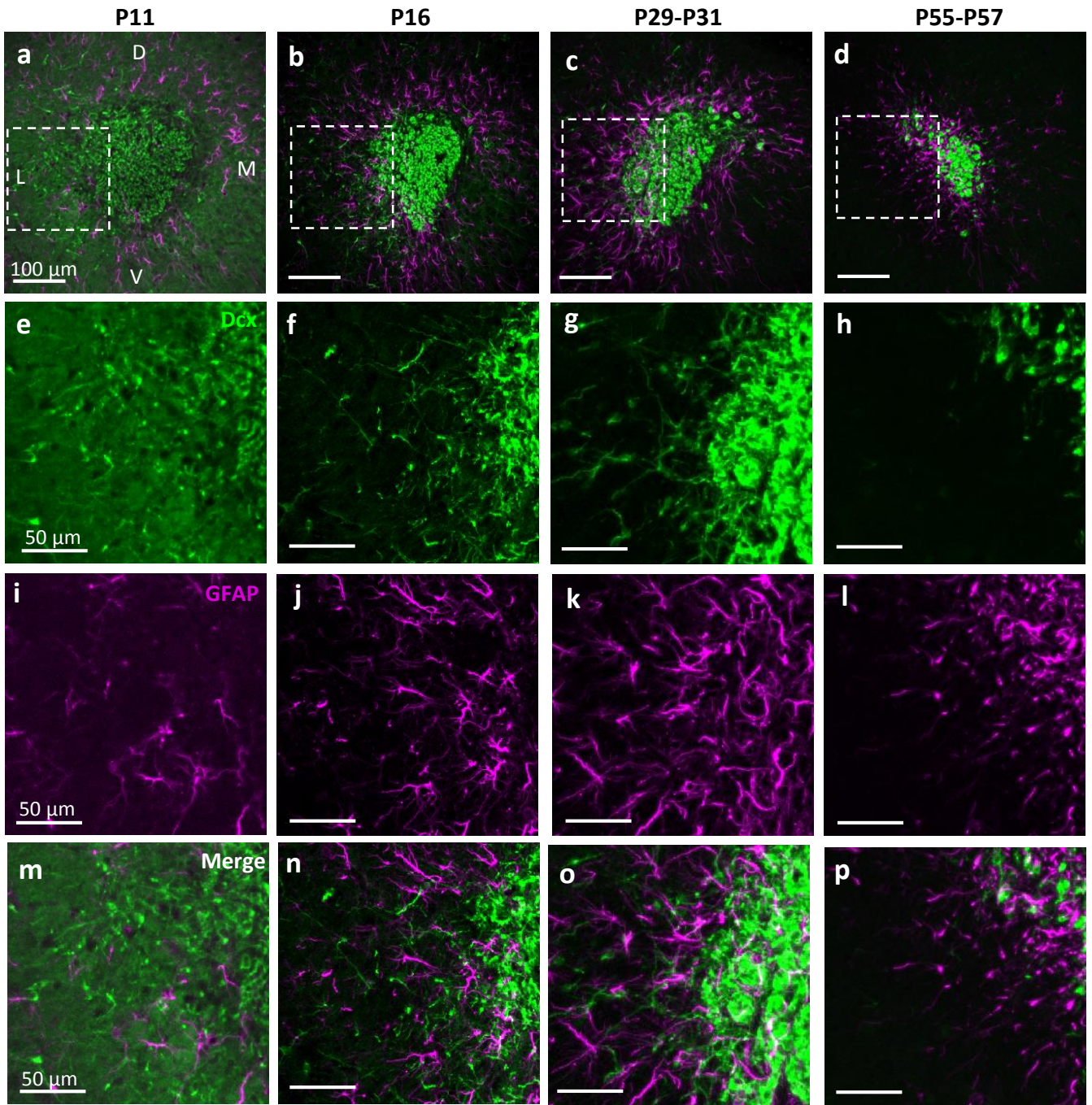


Figure 2

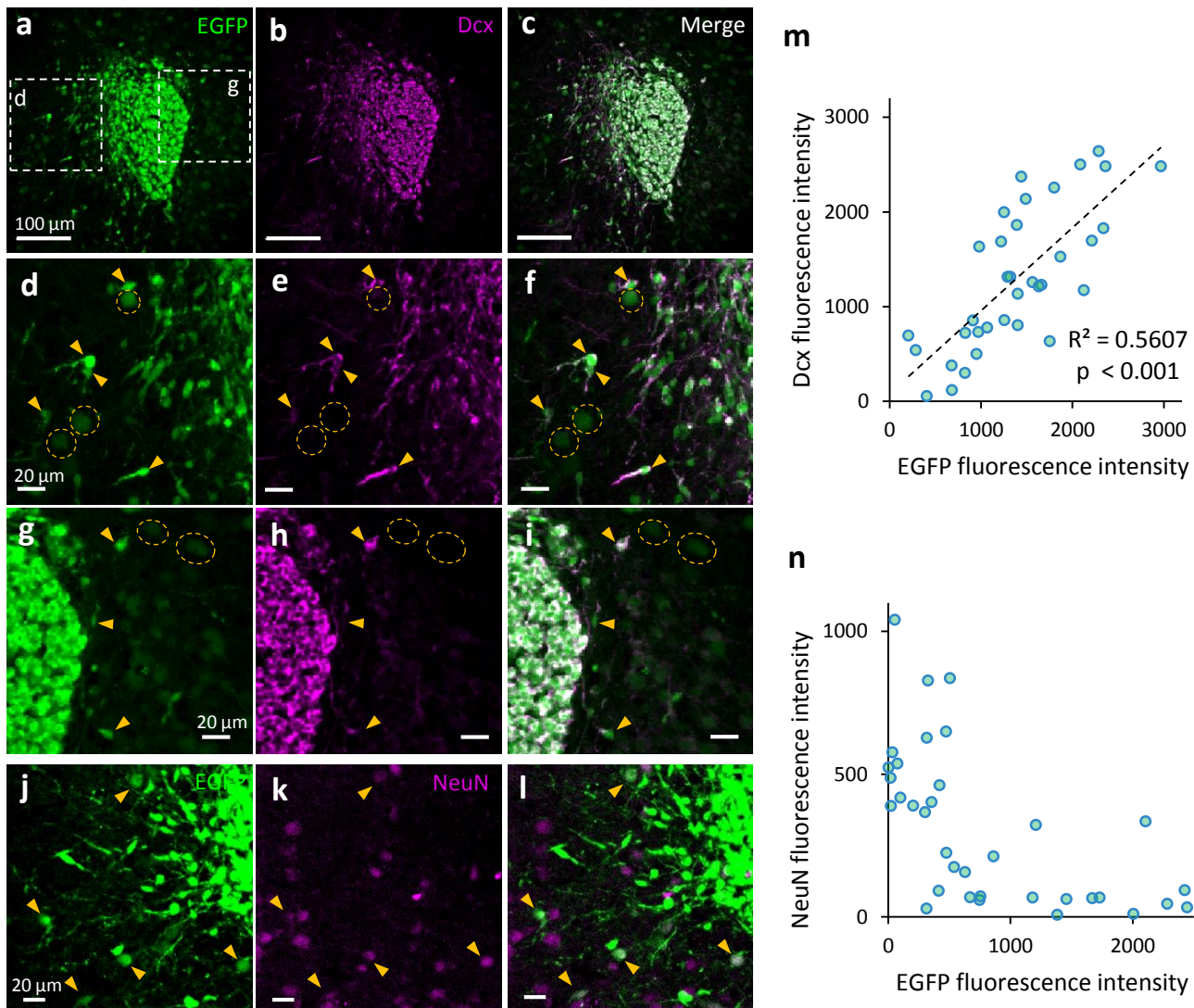


Figure 3

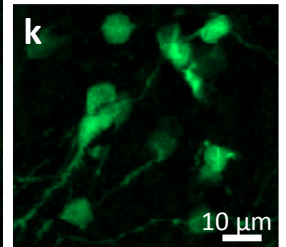
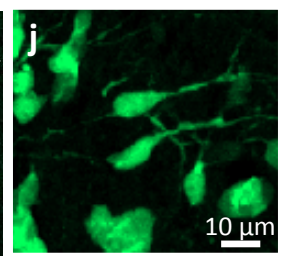
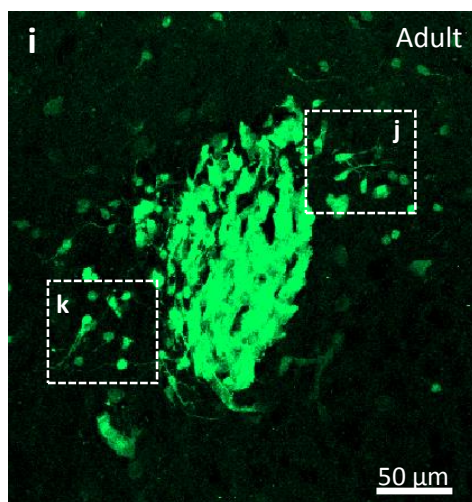
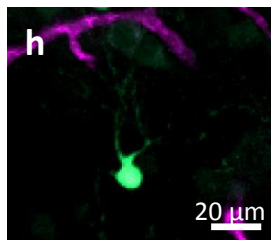
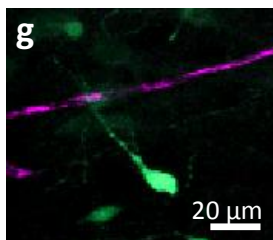
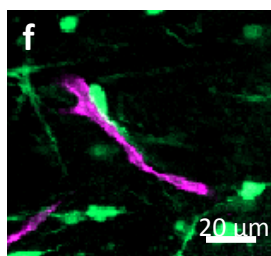
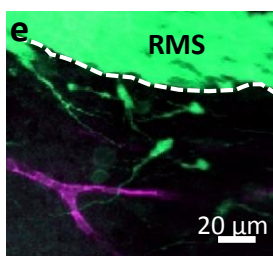
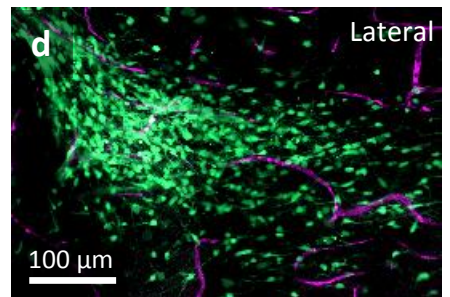
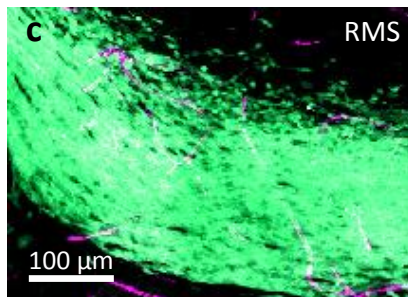
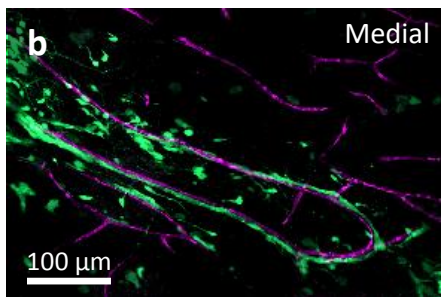
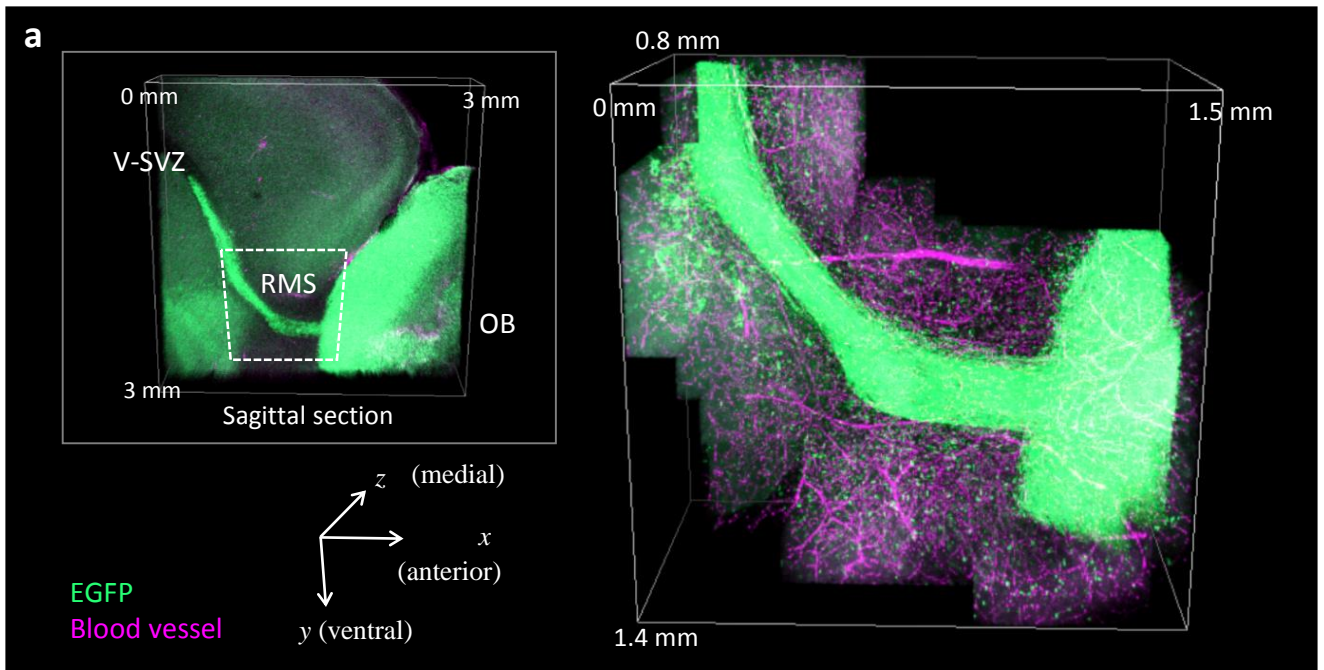


Figure 4

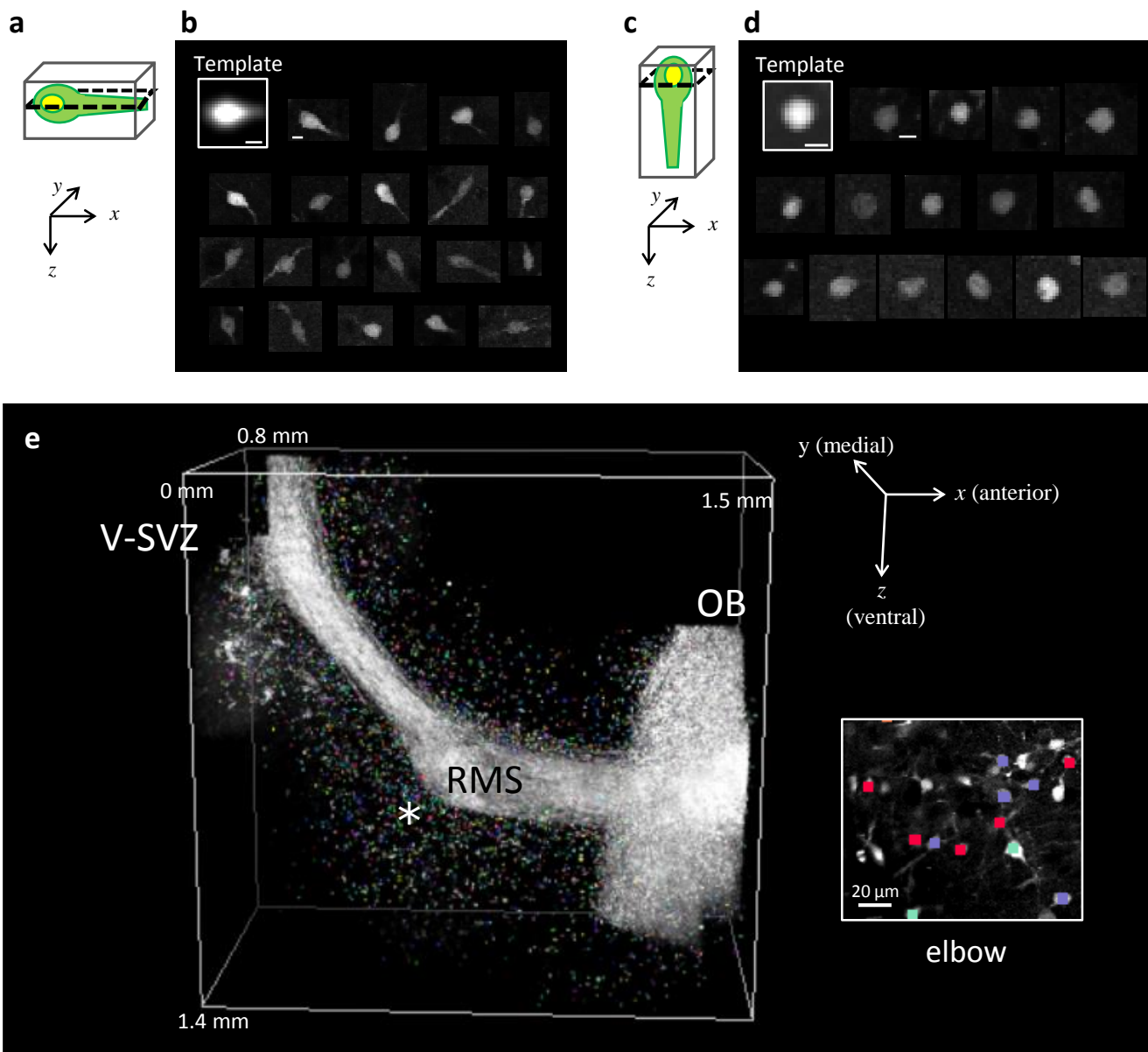


Figure 5

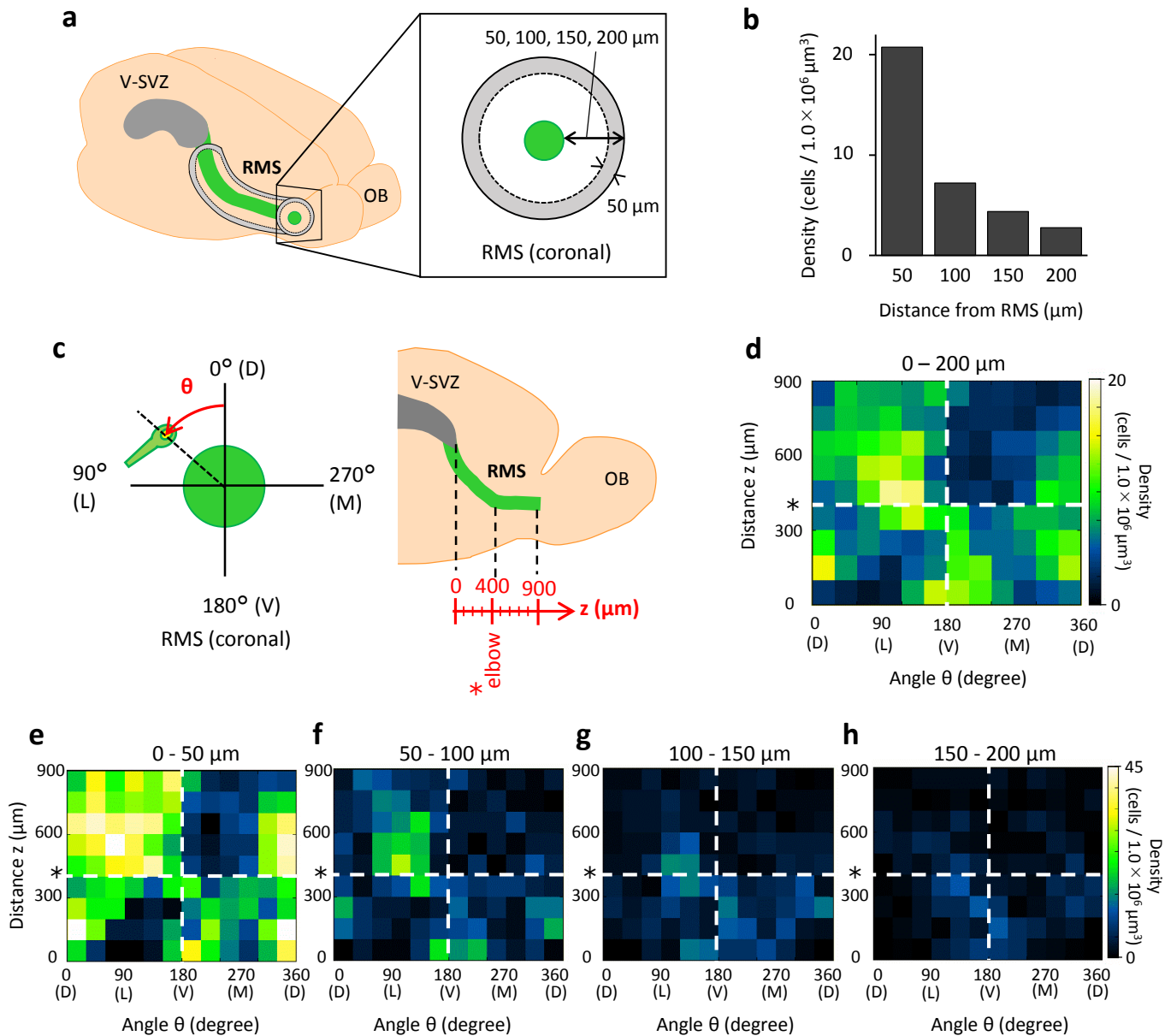


Figure 6

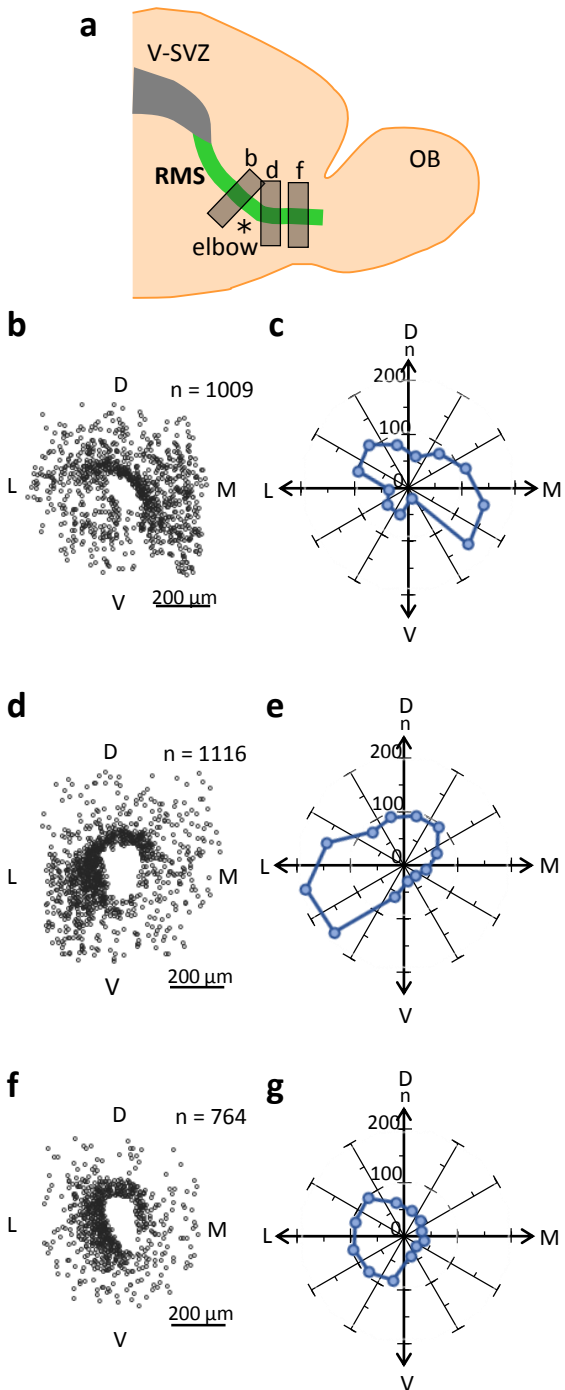


Figure 7

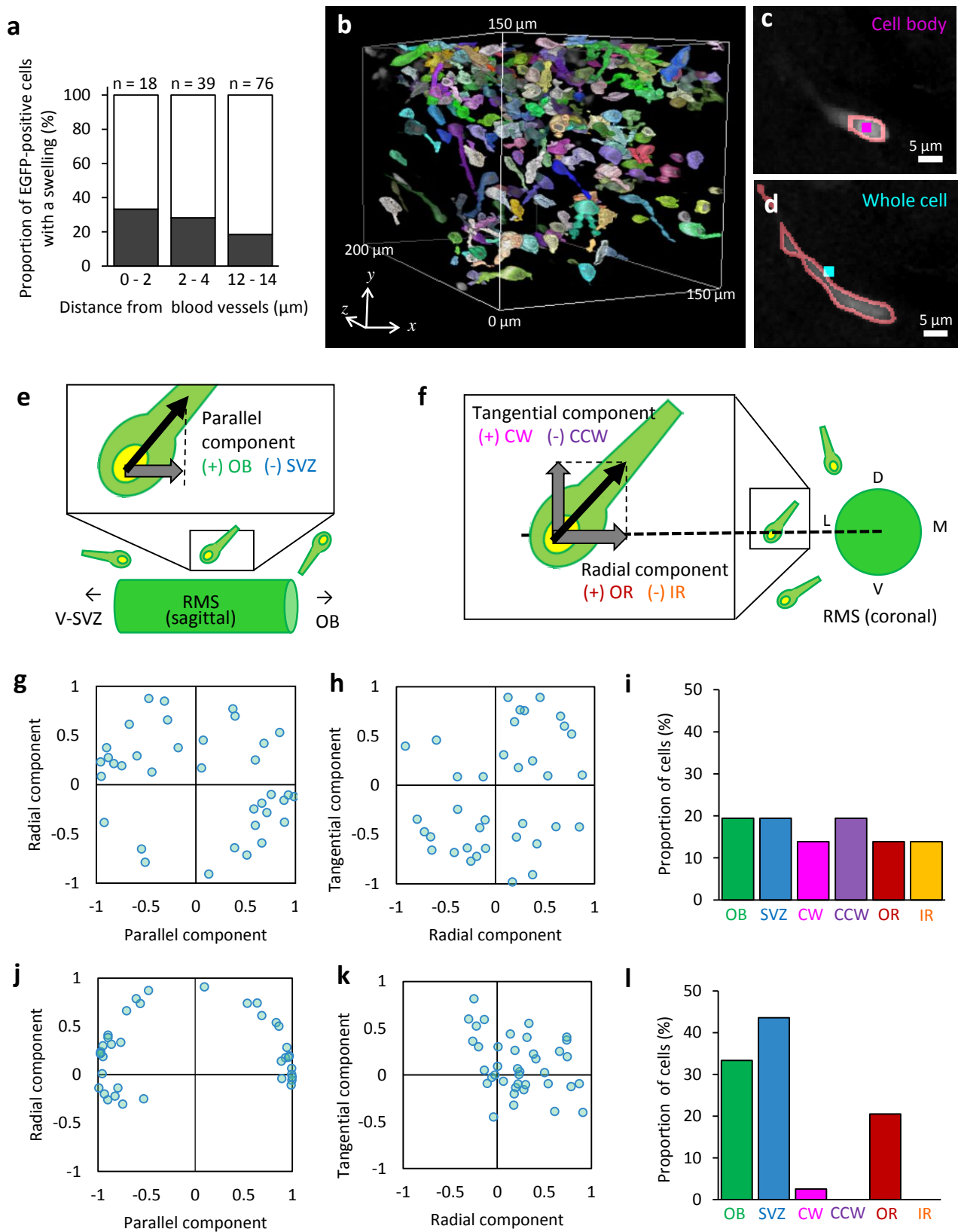


Figure 8

